2D phase field modeling of sintering of silver nanoparticles

2D Phase field modeling of sintering of silver nanoparticles

K. Chockalingam[a], V. G. Kouznetsova[a,*], O. van der Sluis[a,b], M.G.D. Geers[a]

[a]*Department of Mechanical Engineering, Eindhoven University of Technology, 5612 AZ, Eindhoven, The Netherlands*
[b]*Philips Research Laboratories, High Tech Campus 34, 5656 AE Eindhoven, The Netherlands*

Abstract

The sintering mechanism of silver nanoparticles is modelled by incorporating surface, volume and grain boundary diffusion in a phase field model. A direction-dependent tensorial mobility formulation is adopted, capturing the fact that diffusion mainly occurs along the directions tangential to the surface of the particle. A finite element framework is applied to solve the governing equations in a fully coupled implicit manner, and the developed framework is demonstrated for particle sintering of equal and unequal sizes as well as at different temperatures. The obtained results are compared with experimental observations, whereby it is shown that the developed material model adequately describes the sintering mechanism of silver nanoparticles.

Keywords: sintering, Cahn-Hilliard, Allen-Cahn, phase field, silver particles, finite elements, tensorial mobility

Dedicated to Professor Christian Miehe on the occasion of his 60th birthday

As one of the leading scientists in the world in computational mechanics, professor Christian Miehe greatly influenced our work. Many of his contributions to the field are groundbreaking, and of great interest for the entire community. Professor Miehe always showed great interest for multi-scale models, micromechanics and advanced computational approaches for damage and fracture. Among these, he pioneered phase field approaches to fracture. Phase field approaches are intrinsically made to deal with problems characterized by non-convexity or to regularize ill-posed problems. Our contribution focuses on the sintering process, which lends itself excellently to phase field modelling. Moreover, sintering defines the microstructural defects and is therefore determinant for the damage and fracture

---

*Corresponding author
Email address:* `v.kouznetsova@tue.nl` (V. G. Kouznetsova)

behaviour. With this open-minded view on this special issue, we dedicate this paper in honor of professor Christian Miehe.

1. Introduction

There is an ever increasing need to enhance the performance of electronic devices as their size is getting smaller and smaller. Improving the heat dissipation mechanism is one of the ways to significantly enhance the performance of electronic devices. Proper heat transfer prevents the occurrence of excessive temperatures thereby increasing the lifetime and reliability of electronic components [1]. In electronic devices, heat is evacuated from an electronic component via an interconnect material to the substrate on which the component is mounted [2]. Interconnect materials are typically referred to as thermal interface materials (TIM). The focus here is on TIMs that are composed of silver nanoparticles. The sintering process used in the making of this TIM has impact on the resulting material structure, and is thus essential to reduce the heat resistance of TIMs to guarantee its reliability [3]. Quantitative modelling of the sintering process is therefore essential in prediction and control of the processing-structure-property-lifetime performance of TIMs

The process of mass transport in solid state sintering is highly complex, and depends on many physical mechanisms, including, but not limited to, viscous flow, vapor transport, surface diffusion, volume diffusion, grain boundary diffusion, and plastic flow [4]. It also depends on processing conditions such as the applied pressure and temperature-time profile. In the present work, only the most dominant mechanisms are considered, which are the surface, volume and grain boundary diffusion under isothermal conditions at different temperatures with no external pressure. Given the fragile nature of the attached micro-electronic components, the considered sinter paste is processed under pressureless conditions.

To model sintering, appropriate choices for the numerical scheme and material parameters are essential. Up to date, the majority of papers in the literature on the modelling of solid state sintering [5–7] have essentially focused on the development of numerical schemes and their qualitative analysis, and have not directly been applied to a realistic material system to make quantitative predictions. This paper tends to close this gap by applying the developed numerical model to study the sintering mechanism of silver nanoparticles. It is thereby illustrated that the material model adequately captures the sintering behavior in a quantitative manner by comparing it with small scale experiments [8].

One of the earliest works on modeling surface and grain boundary diffusion was performed by Zhang and Schneibel [9], who studied the sintering of two equal circular particles, while monitoring the growth rate exponent and change in neck

size. Later, Pan et al. [10] proposed a numerical scheme to model sintering of particles of different sizes and found that the particle size can influence grain growth and densification. Since then, considerable efforts have been made to model solid state sintering, especially using sharp interface models. Bruchon et al. [5] used a level-set approach to track particle boundaries and demonstrated surface transport in 3D. A discrete element formulation was adopted by Wakai and Brakke [11] to capture surface and grain boundary diffusion. Probabilistic methods have been used by Tikare et al. [12] using a kinetic Monte Carlo model for the sintering of three particles.

Departing from the aforementioned methods, progress has been made in diffuse interface models, e.g. using a phase field approach. Jing et al. [13] used a phase field method to capture pore spheroidization between four particles. The system was solved using a semi-implicit Fourier-Spectral method. A vacancy diffusion approach to model sintering was proposed by Asp and Agren [14], where the solid fraction contained little vacancies and the voids were considered as vacancy rich; this approach can serve as a generic scheme that can be extended to multiphase materials. Wang [6] also incorporated rigid body translation and rotation in the phase field model to capture solid state sintering. Sintering of two unequal-size particles was studied by Kumar et al. [7], who particularly monitored the grain boundary migration during different stages of sintering. A phase field approach has the ability to model complex geometries without the need to explicitly track the interface as in sharp interface models. On the other hand, one of the main limitations of the phase field method over sharp interface models is the diffuse nature of its interface. Grain boundaries are an example of such interfaces, which are rather sharp, whereby a diffuse interface approximation can have a quantitative effect on grain growth prediction [15]. In the case of surface diffusion, this limitation can be partially mitigated through the introduction of an anisotropic tensorial mobility that better approximates the sharp interface equations, as demonstrated by Gugenberger el al. [16]. A similar tensorial mobility correction for grain boundary diffusion is proposed by Moelans et al. [17]. These modifications have been successfully adopted by Deng [18] for two particle sintering, who has highlighted the significance of direction-dependent tensorial mobility effects.

In this work, a finite element based phase field method is used as the numerical scheme for spatial discretization as it offers a large flexibility in capturing the complex nature of sintering. Moreover, finite elements are not restricted to geometries of rectilinear simulation domains. Finite elements have previously been employed [15] to solve well-known phase field equations, i.e. the fourth-order Cahn-Hilliard equation and the second-order Allen-Cahn equation to study spinodal decomposition and grain growth, respectively. The chemical diffusion mobilities used were constant scalars with no directional dependence. The phase field module was

3

programmed within MOOSE [19], an object oriented finite element based non-linear solver. The current work also employs MOOSE to incorporate the sintering module in order to capture the three dominant diffusion mechanisms and grain boundary migration. The chemical diffusion mobilities are taken as functions of the conserved concentration field and the non-conserved order parameter. Tensorial mobility effects are included as a part of the formulation, so that diffusion occurs only along the tangential direction of the particle thereby producing the correct neck growth between sintered particles. In a recent paper by Tonks et al. [20] a finite element scheme including tensorial mobility was employed to study grain boundary pinning and pore interaction.

Most of the above mentioned sintering models rely on a qualitative verification of the sintering process with little emphasis on the material model. Muñoz et al. [21, 22] have proposed a Eulerian finite element framework based level-set method to model multi-particle sintering of alumina particles in 3D, but without any experimental validation. In case of silver, the surface diffusion coefficient [23, 24] and grain boundary mobility coefficient [25, 26] reported in the literature differ by many orders of magnitude, and without proper validation quantitative predictions using the developed numerical scheme would not be possible. After an extensive literature study to identify all necessary material parameters, the results from the model proposed in this paper are in good agreement with theoretical predictions on sintering [4] and experimental observations on silver nanoparticles [8]. Apart from a molecular dynamics simulation by Alarifi et al. [27], the literature does not seem to report other modelling work on sintering of silver particles. Molecular dynamics simulations are highly limited by their length and time scales to simulate any realistic neck growth. The phase field model developed here can be readily extended to continuum length and time scales as required for practical purposes.

In section 2, the phase field model is outlined and all the related quantitative material parameters used in the free energy functional are identified. In section 3, the finite element framework for the fully coupled implicit system of governing equations is presented. In section 4, the developed model is tested for sintering two particles of unequal size. In section 5, the choice of material parameters is discussed and the quantitative results on sintering of silver particles are presented. The paper closes with a discussion and conclusions.

2. Phase field model

In this work, diffusional mass transport and grain boundary migration between sintered silver particles are modeled using the phase field method. For this purpose, a conserved field parameter c and a non-conserved order parameter η_α are introduced, where α is the index of a particle. The conserved field c describes

the concentration of silver, and it takes a value of 1 in the solid phase and 0 in the "void" phase. Here, the conserved concentration field c corresponds to the mass density ρ. The morphological evolution of the particles is described by the non-conserved order parameter η_α. The parameter η_α equals 1 at the αth particle and zero elsewhere in the system. The microstructural evolution is driven by the minimization of the free energy functional which is given by

$$F = \int_v \left\{ f(c, \eta_\alpha) + \frac{1}{2}\kappa_c |\nabla c|^2 + \frac{1}{2}\sum_{\alpha=1}^N \kappa_\eta |\nabla \eta_\alpha|^2 \right\} dv, \qquad (1)$$

where $f(c, \eta_\alpha)$ is the bulk free energy energy, κ_c is the gradient energy parameter for the conserved field, κ_η is the gradient energy parameter for the non-conserved field and N is the total number of order parameters. The following form for the bulk free energy contribution is adopted [6]

$$f(c, \eta_\alpha) = \omega c^2 (1 - c)^2 + \zeta \left[c^2 + 6(1 - c)\sum_{\alpha=1}^N \eta_\alpha^2 - 4(2 - c)\sum_{\alpha=1}^N \eta_\alpha^3 + 3\left(\sum_{\alpha=1}^N \eta_\alpha^2\right)^2 \right], \qquad (2)$$

where ω and ζ are constants. The bulk energy adopted in (2) is the chemical free energy describing homogeneous coexisting phases (solid and pore) and multiple solid domains (nanoparticles). The above Landau-type potential ensures that stable minima in both the solid and void phase are achieved. The constants ω and ζ define the grain boundary energy γ_{gb} and surface energy γ_{sf}, as will be specified in the following.
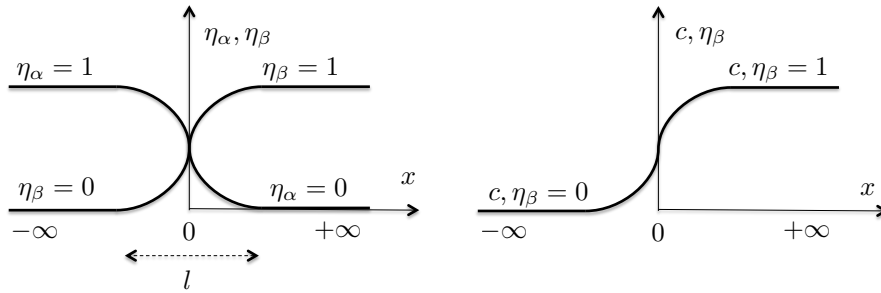
Figure 1: The variation of the non-conserved and conserved parameter at the grain boundary and surface.

The grain boundary energy γ_{gb} at the interface between two particles η_α and η_β in an idealised system of infinite length as seen in Figure 1 can be defined as [17]

$$\gamma_{gb} = \int_{-\infty}^{\infty} \left[f\left(c = 1, \eta_\alpha, \eta_\beta\right) + \frac{\kappa_\eta}{2}\left\{ \left(\frac{d\eta_\alpha}{dx}\right)^2 + \left(\frac{d\eta_\beta}{dx}\right)^2 \right\} \right] dx. \qquad (3)$$

5

Likewise, the surface energy γ_{sf} at the interface between solid and void phases can be defined as [28]

$$\gamma_{sf} = \int_{-\infty}^{\infty} \left[f\left(c, \eta_\beta\right) + \frac{\kappa_c}{2}\left(\frac{dc}{dx}\right)^2 + \frac{\kappa_\eta}{2}\left(\frac{d\eta_\beta}{dx}\right)^2 \right] dx. \tag{4}$$

Ahmed et al. [28] used a quantitative analysis procedure [17] to relate the gradient energy parameters and the constants in the free energy functional (1) to material properties. The analysis is carried out such that the relations between the parameters minimize (3) and (4). The relationships presented in [28] are adopted here

$$\gamma_{gb} = \frac{2}{\sqrt{3}}\sqrt{\zeta\kappa_\eta}, \tag{5}$$

$$\gamma_{sf} = \frac{\sqrt{2}}{6}\sqrt{\kappa_c + \kappa_\eta}\sqrt{\omega + 7\zeta}, \tag{6}$$

$$l = \sqrt{\frac{4\kappa_\eta}{3\zeta}}, \tag{7}$$

where l is the width of the grain boundary.

For the sake of completeness (5) and (7) are derived here and (6) can be obtained following the same procedure. For a grain boundary in local equilibrium, the profiles $\eta_\alpha(x)$ and $\eta_\beta(x)$ adopt a shape that minimizes functional (3) and satisfies the boundary conditions

$$n_\alpha = 1 \quad \text{and} \quad n_\alpha = 0 \quad \text{for} \quad x \to -\infty, \tag{8a}$$

$$n_\beta = 0 \quad \text{and} \quad n_\beta = 1 \quad \text{for} \quad x \to +\infty, \tag{8b}$$

$$\frac{d\eta_\alpha}{dx} = \frac{d\eta_\beta}{dx} = 0 \quad \text{for} \quad x \to \pm\infty. \tag{8c}$$

According to principles of calculus of variation, the Euler equations of (3) must be satisfied

$$\frac{\partial f\left(c = 1, \eta_\alpha, \eta_\beta\right)}{\partial \eta_\alpha} - \kappa_\eta \left(\frac{d^2\eta_\alpha}{dx^2}\right) = 0, \tag{9}$$

$$\frac{\partial f\left(c = 1, \eta_\alpha, \eta_\beta\right)}{\partial \eta_\beta} - \kappa_\eta \left(\frac{d^2\eta_\beta}{dx^2}\right) = 0. \tag{10}$$

Making use of the Beltrami identity (see Appendix A), (9) and (10) can be written as

$$f - \frac{\kappa_\eta}{2}\left[\left(\frac{d\eta_\alpha}{dx}\right)^2 + \left(\frac{d\eta_\beta}{dx}\right)^2\right] = 0. \tag{11}$$

6

Since the free energy functional (1) is symmetric with respect to $\eta_\alpha(x)$ and $\eta_\beta(x)$ the profiles satisfy

$$\eta_\beta = 1 - \eta_\alpha, \tag{12}$$

which in turn gives the following the relation

$$\frac{d\eta_\alpha}{dx} = -\frac{d\eta_\beta}{dx}, \tag{13}$$

and equivalently,

$$\frac{d\eta_\alpha}{d\eta_\beta} = -1. \tag{14}$$

Rearranging (11) and using boundary conditions (8a) to (8c) yields

$$\frac{d\eta_\alpha}{dx} = -\sqrt{\frac{2f}{\kappa_\eta \left[1 + \left(\frac{d\eta_\beta}{d\eta_\alpha}\right)^2\right]}}, \tag{15}$$

$$\frac{d\eta_\beta}{dx} = \sqrt{\frac{2f}{\kappa_\eta \left[1 + \left(\frac{d\eta_\alpha}{d\eta_\beta}\right)^2\right]}}. \tag{16}$$

Substituting (11) into (5) gives

$$\gamma_{gb} = \int_{-\infty}^{+\infty} 2f\left(c = 1, \eta_\alpha, \eta_\beta\right) dx. \tag{17}$$

The bulk free energy is obtained by substituting (12) in (2)

$$f\left(c = 1, \eta_\alpha, \eta_\beta = 1 - \eta_\alpha\right) = 12\zeta\eta_\alpha^2 \left(1 - \eta_\alpha\right)^2. \tag{18}$$

Changing the independent variable in (17) from x to η_α and making use of (15) results in

$$\begin{aligned}
\gamma_{gb} &= 2\int_0^1 f\left(\eta_\alpha, \eta_\beta\left(\eta_\alpha\right)\right) \frac{dx}{d\eta_\alpha} d\eta_\alpha \\
&= \sqrt{2\kappa_\eta} \int_0^1 \sqrt{f\left(c = 1, \eta_\alpha, \eta_\beta\left(\eta_\alpha\right)\right)} \sqrt{1 + \left(\frac{d\eta_\beta\left(\eta_\alpha\right)}{d\eta_\alpha}\right)^2} d\eta_\alpha \tag{19} \\
&= 2\sqrt{12C\kappa_\eta} \int_0^1 \eta_\alpha\left(1 - \eta_\alpha\right) d\eta_\alpha = \frac{2}{\sqrt{3}} \sqrt{\zeta\kappa_\eta}.
\end{aligned}$$

The width of the grain boundary can be calculated by making use of the absolute value of the gradient of $\eta_\alpha(x)$ at $x = 0$

$$\begin{aligned}
l &= \left|\left(\frac{d\eta_\alpha}{dx}\right)_{x=0}\right|^{-1} \\
&= \sqrt{\frac{\kappa_\eta}{f\left(\eta_\alpha = 0.5\right)}} = \sqrt{\frac{4\kappa_\eta}{3\zeta}}.
\end{aligned} \tag{20}$$

7

According to [28], the following relationship must also be satisfied

$$6\zeta/\kappa_\eta = (\omega + \zeta)/\kappa_c, \tag{21}$$

so that all the free energy functional parameters in (1) are uniquely determined.

The conserved field c is evolved using the Cahn-Hilliard equation

$$\begin{aligned} \frac{\partial c}{\partial t} &= \nabla \cdot \left(\mathbf{M} \cdot \nabla \frac{\delta F}{\delta c\,(\mathbf{x}, t)} \right) \\ &= \nabla \cdot \left(\mathbf{M} \cdot \nabla \left(\frac{\partial f}{\partial c} - \kappa_c \nabla^2 c \right) \right), \end{aligned} \tag{22}$$

where $\mathbf{M}$ is the concentration mobility tensor, $\mathbf{x}$ is the spatial position vector and t is the time. The concentration mobility is defined such that Fick's law of diffusion is recovered in the bulk [29]. This can be achieved by defining the concentration mobility as

$$\mathbf{M} = \mathbf{D} \Big/ \left. \frac{\partial^2 F}{\partial c^2} \right|_{c=1} = \mathbf{D} / \left(2 \left(\zeta + \omega \right) \right), \tag{23}$$

where $\mathbf{D}$ is the diffusivity tensor. It is defined as the sum of the contributions from volume, surface, and grain boundary diffusion [20]

$$\mathbf{D} = \mathbf{D}^v + \mathbf{D}^s + \mathbf{D}^{gb}. \tag{24}$$

The diffusivity tensors for volume, surface and grain boundary are defined as

$$\mathbf{D}^v = D^v_{eff} \mathbf{I}, \tag{25}$$

$$\mathbf{D}^s = D^s_{eff} c^2 \left(1 - c^2 \right) \mathbf{T}^s, \tag{26}$$

$$\mathbf{D}^{gb} = D^{gb}_{eff} \sum_{\alpha=1}^{N} \sum_{\beta \neq \alpha}^{N} \eta_\alpha \eta_\beta \mathbf{T}^{gb}, \tag{27}$$

where D^v_{eff}, D^s_{eff}, and D^{gb}_{eff} are the volume, surface and grain boundary diffusion coefficients, respectively, $\mathbf{I}$ is the identity tensor, $\mathbf{T}^s$ is the projection tensor for surface diffusion and $\mathbf{T}^{gb}$ is the projection tensor for grain boundary diffusion, defined in [18] as

$$\mathbf{T}^s = \mathbf{I} - \frac{\nabla c}{\|\nabla c\|} \otimes \frac{\nabla c}{\|\nabla c\|}, \tag{28}$$

$$\mathbf{T}^{gb} = \mathbf{I} - \frac{\nabla \eta_\alpha - \nabla \eta_\beta}{\|\nabla \eta_\alpha - \nabla \eta_\beta\|} \otimes \frac{\nabla \eta_\alpha - \nabla \eta_\beta}{\|\nabla \eta_\alpha - \nabla \eta_\beta\|}, \tag{29}$$

respectively, where ‖.‖ is the Euclidean norm and $\otimes$ represents the dyadic product. The bulk diffusion is assumed to be constant in the entire domain, any contribution to the surface and grain boundary diffusion is negligible as the surface and grain boundary diffusion coefficients are typically many orders larger than that of bulk diffusion coefficient. The surface diffusion is only present at the surface of the particle as the function in (26) is zero in the interior of the solid and void phase. Likewise, grain boundary diffusion is activated if the particles are touching each other as the summation on $\eta_\alpha \eta_\beta$ in (27) is non-zero only in that case. The projection tensor negates any normal component and projects only the tangential components of the diffusion tensor to the surface of the particle.

The non-conserved field η_α is evolved using the Allen-Cahn equation

$$
\begin{aligned}
\frac{\partial \eta_\alpha}{\partial t} &= -L \frac{\delta F}{\delta \eta_\alpha (\mathbf{x}, t)} \\
&= -L \left(\frac{\partial f}{\partial \eta_\alpha} - \kappa_\eta \nabla^2 \eta_\alpha \right),
\end{aligned}
\tag{30}
$$

where L is the order parameter scalar mobility, which can be defined as [17]

$$
L = \frac{\vartheta_{gb} \gamma_{gb}}{\kappa_\eta},
\tag{31}
$$

where ϑ_{gb} is the grain boundary mobility.

It is noted that the kinetic equations (22) and (30) do not incorporate the rigid-body motion as suggested by Wang [6]. Rigid body motion and rotation of particles accompany the shrinkage due to sintering and its effect may be significant in the presence of grain anisotropy and free surfaces. Sintering of thin-films mounted on a substrate, which is of primary interest for the application considered here, constrains the shrinkage, rendering the rigid body motion of the particles to a minimum [30]. Hence, rigid body motion is not included in this work, but should certainly be considered in future extensions of the model.

3. Finite element formulation

In this section, the finite element formulation to solve the Cahn-Hilliard and Allen-Cahn equations is presented. The derivation takes into account that the concentration mobility tensor is a function of both the conserved and non-conserved fields. From here onwards, the abstract tensorial representation used in the previous section is replaced by the index presentation on the spatial domain.

The Cahn-Hilliard equation (22) is a fourth-order equation and can be solved by splitting the equation into two second-order equations [31–33]. This introduces

9

an additional field variable μ. The following two second-order equations result

$$\frac{\partial c}{\partial t} = \frac{\partial}{\partial x_i}\left(M_{ij}\frac{\partial \mu}{\partial x_j}\right), \tag{32}$$

$$\mu = \frac{\partial f}{\partial c} - \kappa_c \frac{\partial^2 c}{\partial x_i \partial x_i}. \tag{33}$$

The weak forms of the residuals R_c and R_μ for (32) and (33), respectively, are obtained by the introduction of the respective trial functions ψ_c and ψ_μ and integration by parts over the volume v of the domain, resulting in

$$R_c = \int_v \frac{\partial c}{\partial t}\psi_c dv + \int_v M_{ij}\frac{\partial \mu}{\partial x_j}\frac{\partial \psi_c}{\partial x_i}dv - \int_\Gamma M_{ij}\frac{\partial \mu}{\partial x_j}\psi_c n_i d\Gamma, \tag{34}$$

$$R_\mu = \int_v \frac{\partial f}{\partial c}\psi_\mu dv - \int_v \mu\psi_\mu dv + \int_v \kappa_c \frac{\partial c}{\partial x_i}\frac{\partial \psi_\mu}{\partial x_i}dv - \int_\Gamma \kappa_c \frac{\partial c}{\partial x_i}\psi_\mu n_i d\Gamma, \tag{35}$$

where n_i is the normal vector to the boundary Γ of the domain.

The second-order Allen-Cahn equation (30), which governs the evolution of the non-conserved field, can be rewritten in the index form as

$$\frac{\partial \eta_\alpha}{\partial t} = -L\left(\frac{\partial f}{\partial \eta_\alpha} - \kappa_\eta \frac{\partial^2 \eta_\alpha}{\partial x_i \partial x_i}\right), \tag{36}$$

giving the weak form of the residual

$$R_{\eta_\alpha} = \int_v \frac{\partial \eta_\alpha}{\partial t}\psi_\eta dv + L\int_v \frac{\partial f}{\partial \eta_\alpha}\psi_\eta dv + L\int_v \kappa_\eta \frac{\partial \eta_\alpha}{\partial x_i}\frac{\partial \psi_\eta}{\partial x_i}dv - L\int_\Gamma \kappa_\eta \frac{\partial \eta_\alpha}{\partial x_i}\psi_\eta n_i d\Gamma, \tag{37}$$

with ψ_η the corresponding test function.

The unknown fields c, μ and η_α are discretized within the finite element setting as

$$c = N_c^I c^I, \quad \mu = N_\mu^I \mu^I, \quad \eta_\alpha = N_\eta^I \eta_\alpha^I, \tag{38}$$

where I denotes the node index and summation on a repeated index is implied; c^I, μ^I and η_α^I are the nodal values and N_c^I, N_μ^I and N_η^I are the corresponding shape functions. Following the standard Galerkin approach, the test functions are discretized as

$$\psi_c = N_c^I \psi_c^I, \quad \psi_\mu = N_\mu^I \psi_\mu^I, \quad \psi_\eta = N_\eta^I \psi_\eta^I, \tag{39}$$

This leads to the discretized residuals

$$R_c^I = \int_v \frac{\partial c}{\partial t}N_c^I dv + \int_v M_{ij}\frac{\partial N_\mu^J}{\partial x_j}\mu^J \frac{\partial N_c^I}{\partial x_i}dv - \int_\Gamma M_{ij}\frac{\partial N_\mu^J}{\partial x_j}\mu^J N_c^I n_i d\Gamma, \tag{40}$$

10

$$R_\mu^I = \int_v \frac{\partial f}{\partial c} N_\mu^I dv - \int_v N_\mu^J \mu^J N_\mu^I dv + \int_v \kappa_c \frac{\partial N_c^J}{\partial x_i} c^J \frac{\partial N_\mu^I}{\partial x_i} dv - \int_\Gamma \kappa_c \frac{\partial N_c^J}{\partial x_i} c^J N_\mu^I n_i d\Gamma, \quad (41)$$

$$R_{\eta_\alpha}^I = \int_v \frac{\partial \eta_\alpha}{\partial t} N_\eta^I dv + L \int_v \frac{\partial f}{\partial \eta_\alpha} N_\eta^I dv + L \int_v \kappa_\eta \frac{\partial N_\eta^J}{\partial x_i} \eta_\alpha^J \frac{\partial N_\eta^I}{\partial x_i} dv - L \int_\Gamma \kappa_\eta \frac{\partial N_\eta^J}{\partial x_i} \eta_\alpha^J N_\eta^I n_i d\Gamma.$$
$$(42)$$

The system of non-linear equations (40)-(42) is solved in a fully-coupled implicit manner using the non-linear solver PETSc [34], which is embedded within the MOOSE [19] framework. The linearization of the residuals (40)-(42) gives for the iterative corrections of the nodal values δc^J, $\delta \mu^J$ and $\delta \eta_1^J, ..., \delta \eta_N^J$

$$
\begin{bmatrix}
\frac{\partial R_c^I}{\partial c^J} & \frac{\partial R_c^I}{\partial \mu^J} & \frac{\partial R_c^I}{\partial \eta_1^J} & \cdots & \frac{\partial R_c^I}{\partial \eta_N^J} \\
\frac{\partial R_\mu^I}{\partial c^J} & \frac{\partial R_\mu^I}{\partial \mu^J} & \frac{\partial R_\mu^I}{\partial \eta_1^J} & \cdots & \frac{\partial R_\mu^I}{\partial \eta_N^J} \\
\frac{\partial R_{\eta_1}^I}{\partial c^J} & \frac{\partial R_{\eta_1}^I}{\partial \mu^J} & \frac{\partial R_{\eta_1}^I}{\partial \eta_1^J} & \cdots & \frac{\partial R_{\eta_1}^I}{\partial \eta_N^J} \\
\vdots & \vdots & \vdots & \ddots & \vdots \\
\frac{\partial R_{\eta_N}^I}{\partial c^J} & \frac{\partial R_{\eta_N}^I}{\partial \mu^J} & \frac{\partial R_{\eta_N}^I}{\partial \eta_1^J} & \cdots & \frac{\partial R_{\eta_N}^I}{\partial \eta_N^J}
\end{bmatrix}
\begin{bmatrix}
\delta c^J \\
\delta \mu^J \\
\delta \eta_1^J \\
\vdots \\
\delta \eta_N^J
\end{bmatrix}
= -
\begin{bmatrix}
R_c^I \\
R_\mu^I \\
R_{\eta_1}^I \\
\vdots \\
R_{\eta_N}^I
\end{bmatrix},
\qquad (43)
$$

with the terms of the Jacobian matrix given in Appendix B.

All simulations were performed using nine-node quadratic elements, which have richer interpolation property compared to computationally cheaper eight-node quadratic elements. Moreover, the use of nine-node elements in combination with operator split version of Cahn-Hilliard equation, instead of Hermite elements used to solve the full Cahn-Hilliard equation, has been recommended by Zhang et al. [31]. Periodic boundary conditions have been applied on all the discretized fields. In the present implementation, the implicit Euler time integration scheme has been used.

4. Test case

To qualitatively validate the model and its implementation, the classical benchmark problem of sintering two particles of unequal size is considered. In this case we set $\omega = 11\zeta$ and $\kappa_c = 2\kappa_\alpha$. The chosen values satisfy relation (21) and give γ_{sf}/γ_{gb} to be 1.5. The surface diffusion coefficient D_{eff}^s is taken as $10^{-16} \mathrm{m}^2 \mathrm{s}^{-1}$. The D_{eff}^{gb}/D_{eff}^s and D_{eff}^v/D_{eff}^s are taken as 10^{-1} and 10^{-3}, respectively. The grain boundary scalar mobility is taken as $\vartheta_{gb} = 10^{-15} \mathrm{m}^4 \mathrm{J}^{-1} \mathrm{s}^{-1}$.

4.1. Sintering of unequal size particles

The particles are initially touching each other and the diameter of the smaller particle is half that of the larger particle as shown in Figure 2a. The evolution of both particles during sintering is shown in Figure 2 as a function of relative time. The evolution of the particles is plotted by computing $\sum_{\alpha=1}^{\alpha=N} \eta_\alpha^2$ in every point of the domain, which takes a value of one at the grains and zero in the voids.

(a) 0.0   (b) 0.01   (c) 0.30
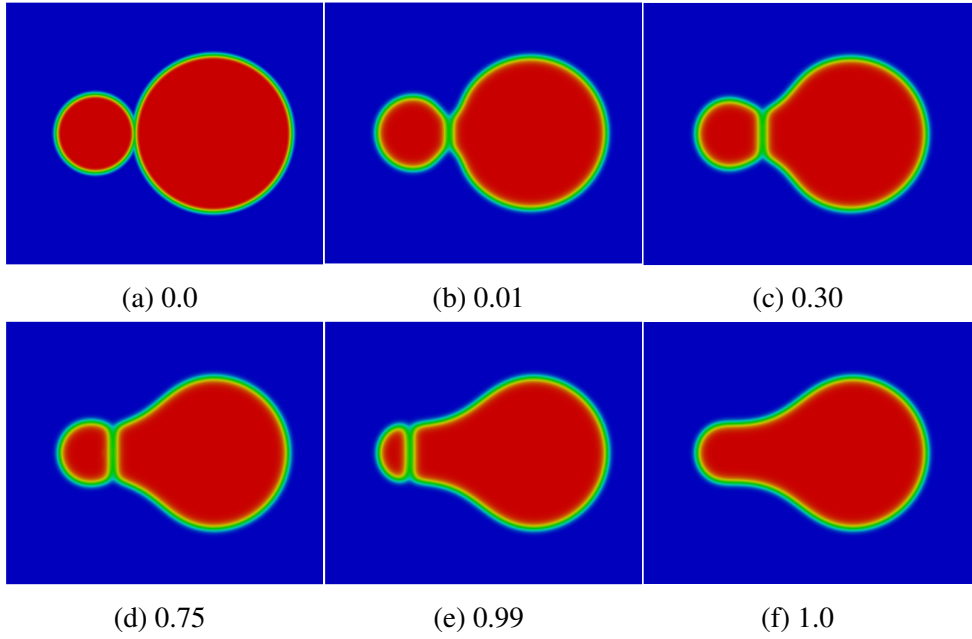
(d) 0.75   (e) 0.99   (f) 1.0

Figure 2: The evolution of two unequal sized particles during sintering at relative times.

The relative neck growth and grain area of the smaller particle are plotted with respect to relative time in Figure 3. The grain area is computed using $\int \eta_\alpha dA$ and the neck growth between particles is approximated as

$$X = \int \left\{ \left(\eta_\alpha \eta_\beta \right) / l \right\} dA, \tag{44}$$

which is non-zero only at the grain boundary. It can be seen that initially there is a rapid neck growth compared to grain growth until time 0.2. After time 0.2 the neck growth continues whereas the smaller grain shrinks. The neck grows to a maximum at approximatively 0.99 relative time, followed by an instantaneous drop to zero neck at time 1.0, corresponding to the disappearance of the smaller grain. These results are consistent with the observations of other phase field models on sintering [7, 28].
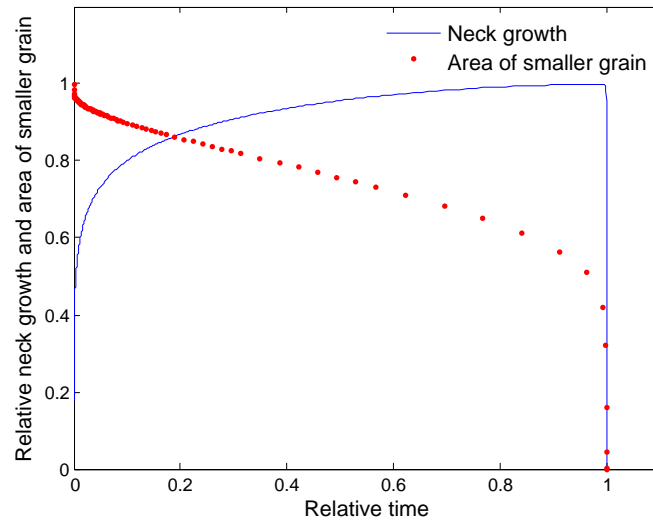
Figure 3: Relative grain area and neck growth as a function of relative time.

4.2. Effect of directional dependent chemical mobility

The same problem with two particles of unequal size as discussed in Section 4.1 is considered but with twice the interface phase width in order to illustrate the effect of the surface projection tensor. In Figure 4 the concentration field for the model with tensor concentration mobility and scalar concentration mobility is plotted for the relative time 0.01. The model with the surface projection tensor, which suppresses any material fluxes perpendicular to the surface of the particle, results in diffusion only tangential to the surface of the particle compared to the model with a scalar concentration mobility that has no directional dependent diffusion. This was also observed by Deng [18].
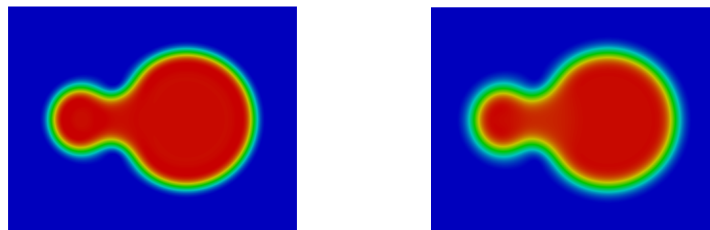
(a) Tensorial concentration mobility   (b) Scalar concentration mobility

Figure 4: The concentration field evolution of two unequal sized particles during sintering at 0.01 relative time, showing the effect of surface diffusion: (a) with tensorial concentration mobility and (b) with scalar concentration mobility.

13

4.3. Adaptive meshing and time stepping

Adaptive meshing and time stepping schemes were adopted to reduce computational costs. The mesh is adapted to the gradient of the solution variables (c, μ, η_α). The mesh depicted in Figure 5 has an initial unadapted mesh size of 2 nm x 2 nm and an interface width of 2 nm. The problem is tested for three levels of h-adaptivity with adaptivity primarily concentrated at the interface. It was found that except for the model with h-level 1 the other two models converged to the expected final solution, i.e. a perfect circle with no smaller grain. Therefore, it has been concluded that the interface has to be resolved by a minimum of four elements to capture any jump in the gradient of the solution variables in order to achieve convergence.

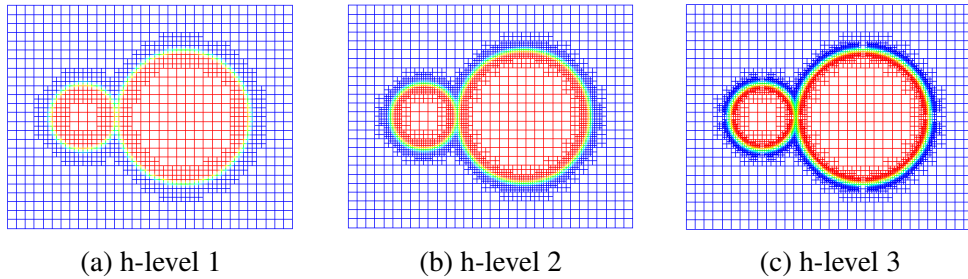

| (a) h-level 1 | (b) h-level 2 | (c) h-level 3 |

Figure 5: Concentration field of two unequal sized particles at 0.0 time with an initial unadapted mesh size of 2 nm x 2 nm and an interface width of 2 nm: (a) h-level 1, (b) h-level 2 and (b) h-level 3.

The adaptive time step corresponding to the two particle system in Section 4.1 is shown in Figure 6. Initially, the time step is small to capture the rapid increase in neck growth followed by an increase of several orders of magnitude, facilitated by the implicit time integration scheme. As there is swift movement of the grain boundary closer to time 1.0 there is again a sudden drop in time step to capture the grain boundary migration. A detailed analysis of the adopted adaptive meshing and time stepping schemes is provided in [15].

5. Sintering of silver particles

In the previous section the model and its finite element implementation were presented and the model was qualitatively verified. Next, the method will be applied to quantitatively study the sintering of silver particles. First, the material model used for silver is presented followed by the results for sintering of silver particles of equal size.
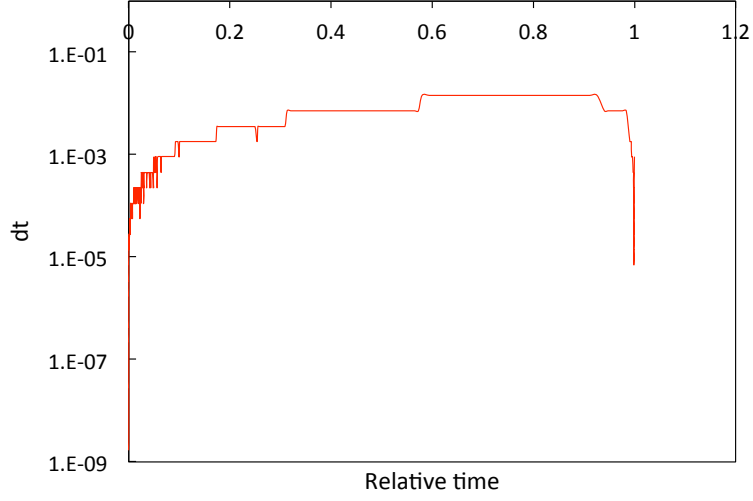
14

Figure 6: Adaptive time step *dt* corresponding to the solution of the two-particle system as a function of relative time.

5.1. Material model

The material parameters required to model sintering of silver particles are the surface diffusion coefficient D_{eff}^s, the volume diffusion coefficient D_{eff}^v, the grain boundary diffusion coefficient D_{eff}^{gb}, the grain boundary mobility ϑ_{gb}, the grain boundary energy γ_{gb} and the surface energy γ_{sf}. The reported grain boundary mobility data of silver in the literature [35–37] reveals a wide range of values with little consistency. The grain boundary mobility for silver is taken from [26], which has a similar order of magnitude compared to other FCC metals like aluminum [38] and copper [39], although the grain boundary mobility is highly dependent on the grain boundary structure which can vary for different metals. The diffusion coefficient D_{eff} obeys the Arrhenius equation

$$D_{eff} = D_o e^{-\frac{Q}{k_b T}}, \tag{45}$$

where T is the temperature, k_b is Boltzmann constant, D_o is a temperature independent constant and Q is the activation energy. The values for D_o and Q for surface and volume diffusion are listed in Table 1. According to [40] the grain boundary diffusion coefficient is typically in between the surface and volume diffusion coefficient and is here taken as 0.1 times surface diffusion coefficient [6, 7, 18]. This is valid for temperatures above 150°C; below 150°C the surface diffusion coefficient tends to approach the volume diffusion coefficient. The material parameters for silver are listed in Table 1. The remaining parameters were determined by solving the systems of equations (5), (6), (7) and (21), which gave the values $\omega = 4.08 \times 10^9 \text{J/m}^3$, $\zeta = 3.95 \times 10^8 \text{J/m}^3$, $\kappa_c = 2.24 \times 10^{-9} \text{J/m}$, $\kappa_\eta = 1.19 \times 10^{-9} \text{J/m}$.

15

Table 1: Material parameters for silver

Propery	Value	Units	Reference
ϑ_{gb}	10^{-16}	$\text{m}^4\text{J}^{-1}\text{s}^{-1}$	[26]
γ_{gb}	0.79	Jm^{-2}	[41]
γ_{sf}	1.14	Jm^{-2}	[25]
Q^s	$(3.84 \pm 0.24) \times 10^{-19}$	J	[24]
D_o^s	$10^{2 \pm 1}$	m^2s^{-1}	[24]
Q^v	$(3.15 \pm 0.16) \times 10^{-19}$	J	[42]
D_o^v	0.67×10^{-4}	m^2s^{-1}	[42]

5.2. Sintering of equal size particles

Two particles of 40 nm diameter are sintered at 400°C and the width of the grain boundary is taken as $l = 2\,\text{nm}$. The phase field model approaches the sharp interface model if the grain size is much larger than the grain boundary width.

The evolution of the silver particles during sintering is compared to the experimental work of Asoro et al. [8]. The comparison is shown in Figure 7 from time 0 to 15 minutes. The phase field plots shown in Figure 7 represent the (conserved) concentration field. An adequate agreement is achieved between the behavior predicted by the phase field model and the experimental observations. A difference, however, can be noticed in the dihedral angle subtended between the particles: as can be seen from Figure 7, the experimental results show that the sintered particles produce an acute dihedral angle [43], whereas the phase field model predicts an obtuse dihedral angle. In the next subsection, it will be investigated which material property influences the dihedral angle. Note, that the presence of carbon impurities on the surface of the silver particle as reported in [8] is not included in the phase field model, even though this may well affect the diffusion coefficient. Moreover, the 2D approximation used in the model may also be responsible for the slight discrepancy between the naturally 3D experiments and the simulation results.

The sintering of particles of equal size can be analyzed in relation to the governing equations for neck growth. The theoretical prediction of neck growth obeys a power law form [4, 6] given by

$$\left(\frac{X}{D}\right)^r = Kt, \tag{46}$$

where r is the growth exponent, D is the particle size and K is a term related to the material properties. The power law is fitted on the computational results, to extract K and r. The relative neck growth and the respective power law fit are
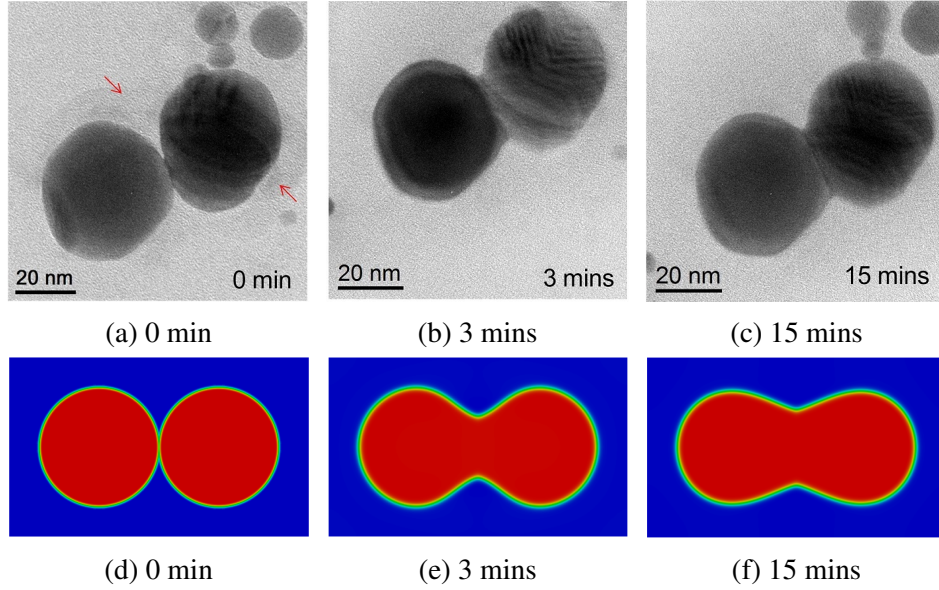
Figure 7: The evolution of two equal sized silver particles of 40 nm in diameter sintered at 400°C for 15 mins. The experimental images shown in (a) through (c) are taken from [8] (reproduced with permission from Elsevier) and the phase field concentration plots are shown in (d) through (f). An adequate comparison between the experimental results and the phase field simulation is established.

shown in Figure 8. As noted in [6] the phase field model at the initial stages of neck growth, may produce certain anomalies due to the large surface curvature involved, and hence the first 1 sec of the neck growth data were not taken into account to prevent any bias. An early stage fit is made for a time less than 2 minutes, and a later stage fit is taken for time instances greater than 2 mins. The growth exponent r is found to be 6.9 for the early stage fit and 7.2 for the later stage fit. Depending on the type of diffusion mechanism, the theoretical value for r can range from 3 to 7 [4] and for certain type of surface diffusion models r can take a value up to 7.5 [4]. Hence, the growth exponent is within the theoretical range.

5.2.1. Dihedral angle

The dihedral angle ϕ subtended between two particles can be defined as [4]

$$\gamma_{sf} = 2\gamma_{gb} \cos\left(\frac{\phi}{2}\right). \tag{47}$$

Thereby changing the γ_{sf}/γ_{gb} ratio, the dihedral angle subtended between the particles can be controlled. In Figure 9 two particles of 15 nm with different γ_{sf}/γ_{gb} ratios sintered at 400°C for 4 mins are shown. In Figure 9a, a γ_{sf}/γ_{gb}
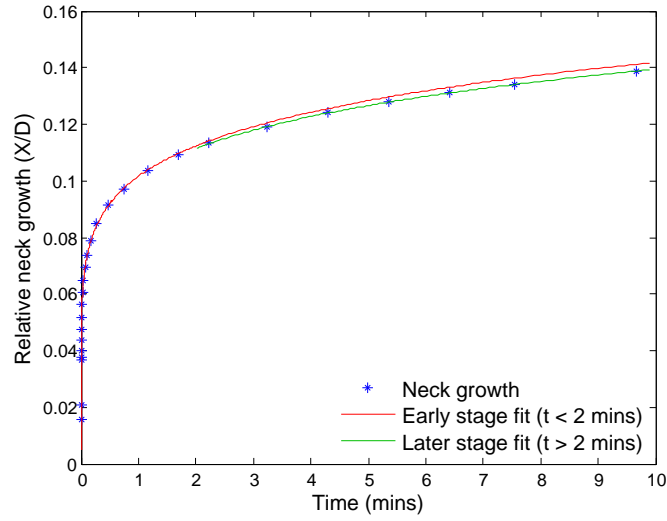
Figure 8: Relative neck growth ratio *X/D* as a function of time and power law fit for different simulation times.

ratio of 1.44 obtained from the grain boundary energy and surface energy values listed in Table 1 for silver is shown to produce a dihedral angle of 139°, whereas a hypothetical γ_{sf}/γ_{gb} ratio of 0.66 is shown to produce a dihedral angle of 83°. Thus, the γ_{sf}/γ_{gb} ratio could have possibly contributed to the difference in the dihedral angle predicted by the phase field model compared to the experimental observation as seen in Figure 7.
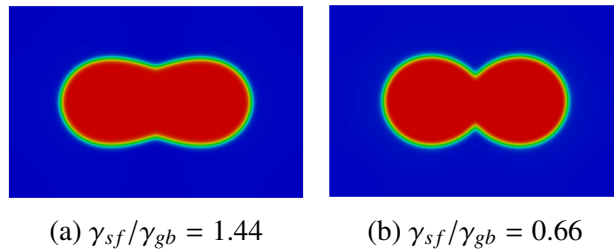

(a) $\gamma_{sf}/\gamma_{gb} = 1.44$ (b) $\gamma_{sf}/\gamma_{gb} = 0.66$

Figure 9: Two 15 nm particles with different γ_{sf}/γ_{gb} ratio sintered at 400°C for 4 mins: (a) for a dihedral angle of 139° and (b) for a dihedral angle of 83°.

5.2.2. Size effect

In order to demonstrate the effect of the absolute size on particle sintering, sintering of particles with a diameter 40 nm and 15 nm at 400°C for 4 mins is simulated. The sintered particles are shown in Figure 10. The relative neck size $\left(\frac{X}{D}\right)$ ratio for the 15 nm particle is higher than for the 40 nm particle, clearly

revealing a size effect. This is due to the higher surface area per unit volume for the smaller particles compared to the larger particles [44], resulting in faster sintering of nanoparticles compared to microparticles.

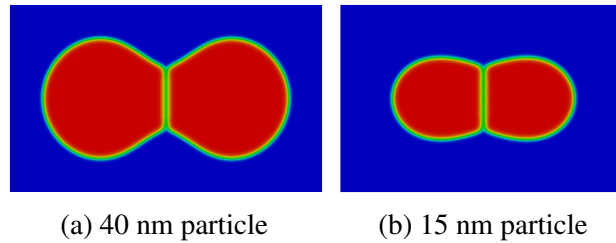(a) 40 nm particle (b) 15 nm particle

Figure 10: Two particles of equal size (a) having a size of 40 nm and (b) having a size of 15 nm sintered at 400°C for 4 mins. Note that the relative neck size (X/D) ratio for the 15 nm particle is larger than for the 40 nm particle, revealing a size effect.

5.2.3. Temperature influence

Finally, the effect of temperature on sintering is analyzed. The technologically relevant temperature range of interest to sinter silver particles is below 400°C. Two silver particles of 15 nm size sintered at 400°C, 300°C and 250°C for four minutes are shown in Figure 11. It can be seen that particles sintered at higher temperatures sinter faster, which is in accordance with the higher diffusion values obeying the Arrhenius equation.
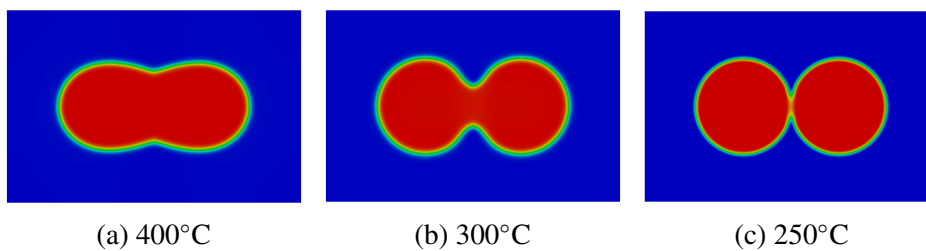

(a) 400°C (b) 300°C (c) 250°C

Figure 11: Two 15 nm particle sintered for 4 mins at three different temperatures at (a) 400°C, (b) 300°C and (c) 250°C. Particles sintered at higher temperature sinter faster.

6. Discussion

The diffusion model (25)-(27), diffusion parameters, energy parameters and grain boundary mobility all influence the diffusion process, rate of diffusion, grain

coarsening, grain boundary migration and the shape of the sintered silver particles. Since the diffusion parameters along with the choice of diffusion model can influence the rate of diffusion, experimental verification of a sintering model is a necessity. As has been shown in section 5.2 there is a good agreement between the experimental observations and the results of the simulations based on the material parameters from the literature, without any fitting parameters. Yet, these material parameters may still be inconsistent with the actual experimental conditions. This may have led to a difference in the dihedral angle predicted by the model compared to the experimental observations, as discussed above. Moreover, other physical processes not accounted for in the model may contribute as well. According to [8, 45], a dislocation-driven plastic flow contribution to neck growth in nanoparticles is not significant as it would require a large stress for plastic flow. Such effects are presently not incorporated. In addition, the effect of the dimensionality, i.e. 2D model versus 3D reality, requires a careful study as well.

7. Conclusion

The main contributions of this paper are:

- A finite element scheme is developed to incorporate the effects of surface, volume and grain boundary diffusion in a phase field sintering model. The implementation is demonstrated for the sintering of two unequal size particles, showing the initial neck growth, followed by coarsening with subsequent slow and rapid grain boundary migration. These observations are in agreement with findings of other phase field sintering models presented in the literature.

- The developed model adequately reproduces the evolution of two silver particles of 40 nm size sintered at $400°$ C, in close agreement with experiment results. All material parameters used were based on values reported in the literature.

- The model can be employed to make quantitative predictions to study multi-particle interaction of silver across an industrially relevant range of length and time scales, as required for practical applications.

A natural extension to the current study would incorporate transient temperature and mechanical effects on the diffusion for further understanding of sintering process. It is noted that anisotropy between the grains is currently not considered and the effect of grain misorientation needs to be investigated in future work. Moreover, the developed model and solution scheme can be applied to study sintering of other materials, under the condition that the material parameters are carefully scrutinized in advance.

8. Acknowledgements

Appendix A.

The Euler equation (9) of (3) is rewritten as

$$\frac{\partial f\left(c = 1, \eta_\alpha, \eta_\beta\left(\eta_\alpha\right)\right)}{\partial \eta_\alpha} - \kappa_\eta \left(\frac{\mathrm{d}^2 \eta_\alpha}{\mathrm{d}x^2}\right) = 0. \tag{A.1}$$

Multiplying (A.1) by $\left(\frac{\partial \eta_\alpha}{\partial x}\right)$ gives

$$\frac{\partial f}{\partial \eta_\alpha}\frac{\partial \eta_\alpha}{\partial x} - \kappa_\eta \frac{\partial \eta_\alpha}{\partial x}\left(\frac{\mathrm{d}^2 \eta_\alpha}{\mathrm{d}x^2}\right) = 0. \tag{A.2}$$

The derivative of f with respect to x can be written as

$$\frac{\mathrm{d}f}{\mathrm{d}x} = \frac{\partial f}{\partial \eta_\alpha}\frac{\partial \eta_\alpha}{\partial x} + \frac{\partial f}{\partial x}. \tag{A.3}$$

Making use of (A.3) in (A.2) we get

$$\left(\frac{\mathrm{d}f}{\mathrm{d}x} - \frac{\partial f}{\partial x}\right) - \kappa_\eta \frac{\partial \eta_\alpha}{\partial x}\frac{\mathrm{d}}{\mathrm{d}x}\left(\frac{\mathrm{d}\eta_\alpha}{\mathrm{d}x}\right) = 0. \tag{A.4}$$

Taking there is no partial derivative of f with respect to x

$$\frac{\mathrm{d}f}{\mathrm{d}x} - \kappa_\eta \frac{\partial \eta_\alpha}{\partial x}\frac{\mathrm{d}}{\mathrm{d}x}\left(\frac{\mathrm{d}\eta_\alpha}{\mathrm{d}x}\right) = 0. \tag{A.5}$$

results in

$$\frac{\mathrm{d}}{\mathrm{d}x}\left(f - \kappa_\eta \frac{\partial \eta_\alpha}{\partial x}\frac{\mathrm{d}\eta_\alpha}{\mathrm{d}x}\right) = 0, \tag{A.6}$$

which gives αct as the constant of integration

$$f - \kappa_\eta \left(\frac{\mathrm{d}\eta_\alpha}{\mathrm{d}x}\right)^2 = \alpha ct. \tag{A.7}$$

Similarly,

$$f - \kappa_\eta \left(\frac{\mathrm{d}\eta_\beta}{\mathrm{d}x}\right)^2 = \beta ct. \tag{A.8}$$

Evaluating at $\pm\infty$ and using the boundary conditions (8a) to (8c) yields the constant of integration to be zero.

Appendix B.

The terms in the Jacobian matrix (43) is given by

$$\frac{\partial R_c^I}{\partial c^J} = \int_v \frac{\partial \dot{c}}{\partial c} N_c^J N_c^I dv + \int_v \frac{\partial M_{ij}}{\partial c} N_c^J \frac{\partial N_\mu^K}{\partial x_j} \mu^K \frac{\partial N_c^I}{\partial x_i} dv - \int_\Gamma \frac{\partial M_{ij}}{\partial c} N_c^J \frac{\partial N_\mu^K}{\partial x_j} \mu^K N_c^I n_i d\Gamma,$$

$$(B.1)$$

$$\frac{\partial R_c^I}{\partial \mu^J} = \int_v M_{ij} \frac{\partial N_\mu^J}{\partial x_j} \frac{\partial N_c^I}{\partial x_i} dv - \int_\Gamma M_{ij} \frac{\partial N_\mu^J}{\partial x_j} N_c^I n_i d\Gamma, \tag{B.2}$$

$$\frac{\partial R_c^I}{\partial \eta_\alpha^J} = \int_v \frac{\partial M_{ij}}{\partial \eta_\alpha} N_\eta^J \frac{\partial N_\mu^K}{\partial x_j} \mu^K \frac{\partial N_c^I}{\partial x_i} dv - \int_\Gamma \frac{\partial M_{ij}}{\partial \eta_\alpha} N_\eta^J \frac{\partial N_\mu^K}{\partial x_j} \mu^K N_c^I n_i d\Gamma, \tag{B.3}$$

$$\frac{\partial R_\mu^I}{\partial c^J} = \int_v \frac{\partial^2 f}{\partial c^2} N_c^J N_\mu^I dv + \int_v \kappa_c \frac{\partial N_c^J}{\partial x_i} \frac{\partial N_\mu^I}{\partial x_i} dv - \int_\Gamma \kappa_c \frac{\partial N_c^J}{\partial x_i} N_\mu^I n_i d\Gamma, \tag{B.4}$$

$$\frac{\partial R_\mu^I}{\partial \mu^J} = \int_v \frac{\partial^2 f}{\partial c \partial \mu} N_\mu^J N_\mu^I dv - \int_v N_\mu^J N_\mu^I dv, \tag{B.5}$$

$$\frac{\partial R_\mu^I}{\partial \eta_\alpha^J} = \int_v \frac{\partial^2 f}{\partial c \partial \eta_\alpha} N_\eta^J N_\mu^I dv, \tag{B.6}$$

$$\frac{\partial R_{\eta_\alpha}^I}{\partial c^J} = L \int_v \frac{\partial^2 f}{\partial c \partial \eta_\alpha} N_c^J N_\eta^I dv, \tag{B.7}$$

$$\frac{\partial R_{\eta_\alpha}^I}{\partial \mu^J} = L \int_v \frac{\partial^2 f}{\partial \mu \partial \eta_\alpha} N_\mu^J N_\eta^I dv, \tag{B.8}$$

$$\frac{\partial R_{\eta_\alpha}^I}{\partial \eta_\alpha^J} = \int_v \frac{\partial \dot{\eta}_\alpha}{\partial \eta_\alpha} N_\eta^J N_\eta^I dv + L \int_v \frac{\partial^2 f}{\partial \eta_\alpha^2} N_\eta^J N_\eta^I dv + L \int_v \kappa_\eta \frac{\partial N_\eta^J}{\partial x_i} \frac{\partial N_\eta^I}{\partial x_i} dv - L \int_\Gamma \kappa_\eta \frac{\partial N_\eta^J}{\partial x_i} N_\eta^I n_i d\Gamma,$$

$$(B.9)$$

$$\frac{\partial R_{\eta_\alpha}^I}{\partial \eta_\beta^J} = L \int_v \frac{\partial^2 f}{\partial \eta_\beta \partial \eta_\alpha} N_\eta^J N_\eta^I dv. \tag{B.10}$$

where $\dot{c} = \partial c / \partial t$ and $\dot{\eta}_\alpha = \partial \eta_\alpha / \partial t$ to which an appropriate time discretization scheme should be applied.

References

[1] H.-M. Tong, Y.-S. Lai, C. Wong, Advanced Flip Chip Packaging, Springer, 2012.

[2] Y. Li, C. Wong, Recent advances of conductive adhesives as a lead-free alternative in electronic packaging: Materials, processing, reliability and applications, Materials Science and Engineering: R: Reports 51 (1–3) (2006) 1 – 35.

[3] T. Wang, X. Chen, G.-Q. Lu, G.-Y. Lei, Low-temperature sintering with nano-silver paste in die-attached interconnection, Journal of Electronic Materials 36 (10) (2007) 1333–1340.

[4] R. M. German, Sintering Theory and Practice, Springer, 1996.

[5] J. Bruchon, S. Drapier, F. Valdivieso, 3D finite element simulation of the matter flow by surface diffusion using a level set method, International Journal for Numerical Methods in Engineering 86 (7) (2011) 845–861.

[6] Y. U. Wang, Computer modeling and simulation of solid-state sintering: A phase field approach, Acta Materialia 54 (4) (2006) 953 – 961.

[7] V. Kumar, Z. Fang, P. Fife, Phase field simulations of grain growth during sintering of two unequal-sized particles, Materials Science and Engineering: A 528 (1) (2010) 254 – 259.

[8] M. Asoro, P. Ferreira, D. Kovar, In situ transmission electron microscopy and scanning transmission electron microscopy studies of sintering of Ag and Pt nanoparticles, Acta Materialia 81 (2014) 173 – 183.

[9] W. Zhang, J. Schneibel, The sintering of two particles by surface and grain boundary diffusion – a two-dimensional numerical study, Acta Metallurgica et Materialia 43 (12) (1995) 4377 – 4386.

[10] J. Pan, H. Le, S. Kucherenko, J. Yeomans, A model for the sintering of spherical particles of different sizes by solid state diffusion, Acta Materialia 46 (13) (1998) 4671 – 4690.

[11] F. Wakai, K. Brakke, Mechanics of sintering for coupled grain boundary and surface diffusion, Acta Materialia 59 (14) (2011) 5379 – 5387.

[12] V. Tikare, M. Braginsky, E. A. Olevsky, Numerical simulation of solid-state sintering: I, sintering of three particles, Journal of the American Ceramic Society 86 (1) (2003) 49–53.

[13] X. Jing, J. Zhao, L. He, 2D aggregate evolution in sintering due to multiple diffusion approaches, Materials Chemistry and Physics 80 (3) (2003) 595 – 598.

[14] K. Asp, J. Ågren, Phase-field simulation of sintering and related phenomena − A vacancy diffusion approach, Acta Materialia 54 (5) (2006) 1241 – 1248.

[15] M. R. Tonks, D. Gaston, P. C. Millett, D. Andrs, P. Talbot, An object-oriented finite element framework for multiphysics phase field simulations, Computational Materials Science 51 (1) (2012) 20 – 29.

[16] C. Gugenberger, R. Spatschek, K. Kassner, Comparison of phase-field models for surface diffusion, Physical Review E 78 (2008) 016703.

[17] N. Moelans, B. Blanpain, P. Wollants, Quantitative analysis of grain boundary properties in a generalized phase field model for grain growth in anisotropic systems, Physical Review B 78 (2008) 024113.

[18] J. Deng, A phase field model of sintering with direction-dependent diffusion, Materials Transactions 53 (2) (2012) 385–389.

[19] D. Gaston, C. Newman, G. Hansen, D. Lebrun-Grandié, MOOSE: A parallel computational framework for coupled systems of nonlinear equations, Nuclear Engineering and Design 239 (10) (2009) 1768 – 1778.

[20] M. R. Tonks, Y. Zhang, A. Butterfield, X.-M. Bai, Development of a grain boundary pinning model that considers particle size distribution using the phase field method, Modelling and Simulation in Materials Science and Engineering 23 (4) (2015) 045009.

[21] D. Pino-Muñoz, J. Bruchon, F. Valdivieso, S. Drapier, Solid-state sintering simulation: surface, volume and grain-boundary diffusions, in: Proceedings of the 6th European Congress on Computational Methods in Applied Sciences and Engineering, 2012, pp. 163–202.

[22] D. Pino-Muñoz, J. Bruchon, S. Drapier, F. Valdivieso, Sintering at particle scale: An Eulerian computing framework to deal with strong topological and material discontinuities, Archives of Computational Methods in Engineering 21 (2) (2014) 141–187.

[23] J. B. Drew, J. J. Pye, Measurements of surface diffusion coefficients on silver single crystal, Transactions of the Metallurgical Society of AIME 227 (1) (1963) 99–102.

[24] G. Rhead, Surface self-diffusion and faceting on silver, Acta Metallurgica 11 (9) (1963) 1035 – 1042.

[25] D. Meclean, Grain Boundaries in Metals, Oxford Press, 1957.

[26] R. Pareja, Migration kinetics of (001) twist grain-boundaries in silver bicrystalline films, Zeitschrift Fur Metallkunde 72 (3) (1981) 198 – 202.

[27] H. A. Alarifi, M. Atis, C. Ozdogan, A. Hu, M. Yavuz, Y. Zhou, Molecular dynamics simulation of sintering and surface premelting of silver nanoparticles, Materials Transactions 54 (6) (2013) 884–889.

[28] K. Ahmed, C. A. Yablinsky, A. Schulte, T. Allen, A. El-Azab, Phase field modeling of the effect of porosity on grain growth kinetics in polycrystalline ceramics, Modelling and Simulation in Materials Science and Engineering 21 (6) (2013) 065005.

[29] P. C. Millett, M. R. Tonks, S. Biner, L. Zhang, K. Chockalingam, Y. Zhang, Phase-field simulation of intergranular bubble growth and percolation in bicrystals, Journal of Nuclear Materials 425 (1–3) (2012) 130 – 135.

[30] Y. Wang, Y. Liu, C. Ciobanu, B. Patton, Simulating microstructural evolution and electrical transport in ceramic gas sensors, Journal of the American Ceramic Society 83 (9) (2000) 2219–2226.

[31] L. Zhang, M. R. Tonks, D. Gaston, J. W. Peterson, D. Andrs, P. C. Millett, B. S. Biner, A quantitative comparison between C^1 and C^0 elements for solving the Cahn−Hilliard equation, Journal of Computational Physics 236 (2013) 74 – 80.

[32] C. Elliott, D. French, F. Milner, A second order splitting method for the Cahn−Hilliard equation, Numerische Mathematik 54 (5) (1989) 575–590, cited By 110.

[33] R. Ubachs, P. Schreurs, M. Geers, A nonlocal diffuse interface model for microstructure evolution of tin–lead solder, Journal of the Mechanics and Physics of Solids 52 (8) (2004) 1763 – 1792.

[34] S. Balay, W. D. Gropp, L. C. McInnes, B. F. Smith, Efficient management of parallelism in object oriented numerical software libraries, in: E. Arge, A. M. Bruaset, H. P. Langtangen (Eds.), Modern Software Tools in Scientific Computing, Birkhäuser Press, 1997, pp. 163–202.

[35] W. Bron, E. Machlin, Grain boundary mobilities in high purity silver, Transactions of the American Institue of Mining and Metallurgical Eingineers 206 (5) (1956) 513–514.

[36] R. Dannenberg, E. Stach, J. Groza, B. Dresser, In-situ TEM observations of abnormal grain growth, coarsening, and substrate de-wetting in nanocrystalline Ag thin films, Thin Solid Films 370 (1–2) (2000) 54 – 62.

[37] Z. T. Trautt, M. Upmanyu, A. Karma, Interface mobility from interface random walk, Science 314 (5799) (2006) 632–635.

[38] M. L. Taheri, D. Molodov, G. Gottstein, A. D. Rollett, Grain boundary mobility under a stored-energy driving force: a comparison to curvature-driven boundary migration, Zeitschrift Fur Metallkunde 96 (10) (2005) 1166–1170.

[39] R. Vandermeer, D. Jensen, E. Woldt, Grain boundary mobility during recrystallization of copper, Metallurgical and Materials Transactions A 28 (3) (1997) 749–754.

[40] D. A. Porter, K. E. Easterling, M. Sherif, Phase Transformations in Metals and Alloys, CRC Press, 2009.

[41] M. C. Inman, H. R. Tipler, Interfacial energy and composition in metals and alloys, Metallurgical Reviews 8 (1) (1963) 105–166.

[42] S. J. Rothman, N. L. Peterson, J. T. Robinson, Isotope effect for self-diffusion in single crystals of silver, Physica Status Solidi (b) 39 (2) (1970) 635–645.

[43] M. A. Asoro, Coalescence and sintering in metallic nanoparticles: In-situ transmission electron microscopy (TEM) study, Ph.D. thesis, University of Texas (2012).

[44] V. Kumar, Simulation and modeling of unequal sized particles sintering, Ph.D. thesis, University of Utah (2011).

[45] Z. W. Shan, R. K. Mishra, S. A. S. Asif, O. L. Warren, A. M. Minor, Mechanical annealing and source-limited deformation in submicrometre-diameter Ni crystals, Nature Materials 7 (2007) 115 – 119.